Supporting information for

Interconnection of smectic domains by polyethylene oxide networks towards efficient and thermally stable dye-sensitized solar cells

Caihong Wang, Xueyong Li, Jiwen Zhou, Wen Tian, Junyi Ji, Shuai Tan* and Yong Wu

School of Chemical Engineering, Sichuan University, No. 24 South Section 1, Yihuan Road, Chengdu 610065, China.

*To whom correspondence should be sent: tanshuai@scu.edu.cn

1. ^{1}H NMR and FT-IR measurements S2

2. Mesomorphic properties of the electrolytes S3

3. Diffusion coefficient of the electrolytes S4

4. Ion conductivity of the electrolytes S5

5. SEM images of the DSSCs S7

6. EIS measurements and *IPCE* spectra of the DSSCs S8

7. Comparisons table of performance and properties S9

Reference S10

1. ^{1}H NMR and FT-IR measurements

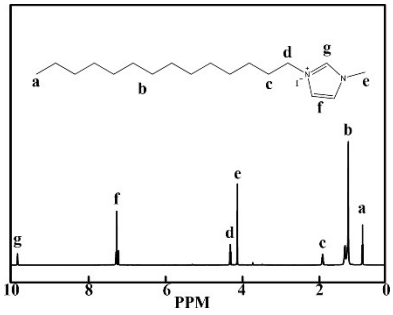

Fig. S1 ^{1}H NMR spectrum of [C_{14}MIm][I]

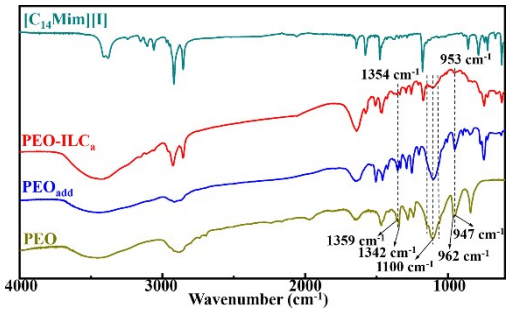

Fig. S2 FT-IR spectra of PEO-ILC$_a$, PEO$_{add}$, [C_{14}Mim][I] and pure PEO

FT-IR measurements of PEO-ILC$_a$, [C_{14}Mim][I], PEO$_{add}$ and pure PEO were also performed and the obtained FT-IR spectra were shown in Figure S2. Triple peaks at around 1100 cm^{-1}, double peaks at around 1350 cm^{-1} and double peaks at around 950 cm^{-1} in the FT-IR spectrum of pure PEO suggested the crystallization of PEO chains[S1]. After adding additives and [C_{14}Mim][I] into PEO, the triple peaks at around 1100 cm^{-1}, the double peaks at around 1350 cm^{-1} and the double peaks at around 950 cm^{-1} were replaced by single peaks centered at 1100 cm^{-1}, 1354 cm^{-1} and 953 cm^{-1}, respectively. These result revealed that the additives and [C_{14}Mim][I] could lowered the crystallinity of PEO chains [S1], which was in agree with the results obtained from XRD measurements. By further comparing the FT-IR spectra of PEO-ILC$_a$, PEO$_{add}$ and [C_{14}Mim][I], no new peak and no chemical band shift was observed in the FT-IR spectrum of PEO-ILC$_a$, which implied that the formation of polymer gel electrolytes containing PEO, [C_{14}Mim][I] and additives was mainly based on physical interactions.

2. Mesomorphic properties of the electrolytes

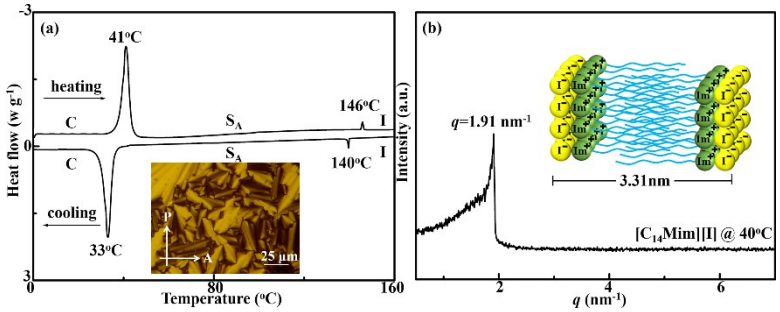

Fig. S3 (a) DSC traces of $[C_{14}Mim][I]$ during the first cooling and second heating process (C: crystal, S_A: smectic A phase, I: isotropic liquid) and POM observation of $[C_{14}Mim][I]$ at 40 °C during cooling process; (b) SAXS pattern of $[C_{14}Mim][I]$ at 40 °C during cooling and the proposed molecular arrangement of smectic $[C_{14}Mim][I]$

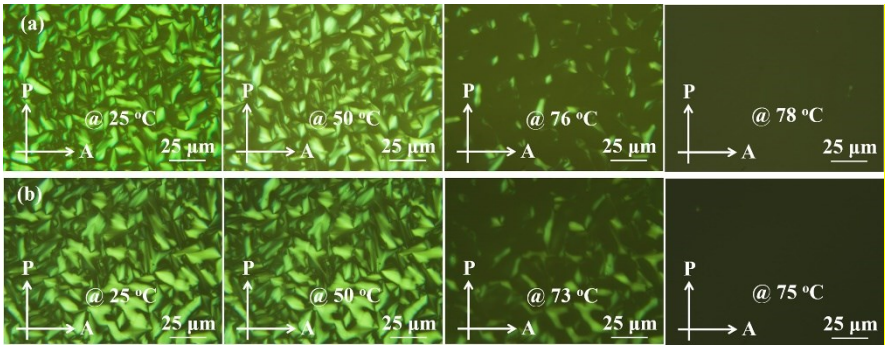

Fig. S4 (a) POM observations of ILC_a (a) and PEO-ILC_a (b) at various temperatures during heating process

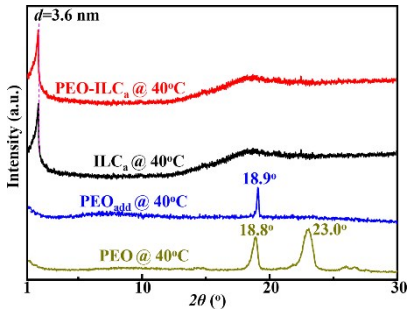

Fig. S5 X-ray diffraction patterns of PEO-ILC_a, ILC_a, PEO_{add} and pure PEO at 40°C

3. Diffusion coefficient of the electrolytes

Diffusion coefficient (D_{app}) of the electrolyte was determined from the limited current (J_{lim}) obtained by CV measurement (scanning rate: 10 mV s^{-1}) using a symmetric cell as described in the literature[S2]. The symmetric cell was prepared by sandwiching the electrolyte between two Pt coated FTO glass electrodes. Temperature of the symmetric cell was controlled by a hot stage. The measured CV curves of the electrolytes at 40 °C are shown in Fig. S6**.** The relationship between D_{app} and J_{lim} is described by equation (S-1).

$$J_{\text{lim}} = \frac{2ne_0 D_{app} C N_A A}{l} \qquad \text{(S-1)}$$

Where n, e_0, C, N_A, l and A denote the number of electrons transferred in the reaction (n=2), the elementary charge (e_0=1.6×10^{-19} C), the charge carrier concentration (mol L^{-1}), the Avogadro constant (N_A=6.02×10^{23} C), the distance between electrodes and the active area of the interface between the electrodes and electrolyte, respectively.

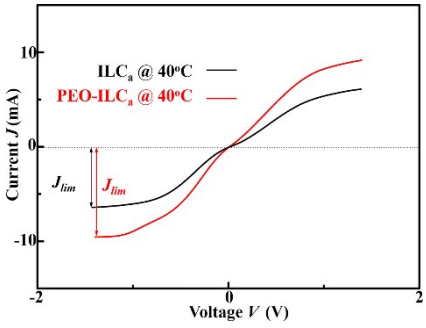

Fig. S6 Cyclic voltammogram curves of the symmetric cells containing ILC_a and PEO-ILC_a at 40 °C

4. Ion conductivity of the electrolytes

The ion conductivities of the electrolyte were determined by EIS measurements using Pt coated FTO glass electrodes or comb-shaped gold electrodes, as schematically illustrated in Fig. S7a. The electrolyte was sandwiched between the substrates to perform the EIS measurements. The temperature of the measured sample was controlled by a hot stage. The Nyquist plots of the symmetric cells obtained from EIS measurements at 0 V bias potential under 40 ^{o}C are shown in Fig. S7b and 7c. On the basis of EIS theory, the ideal Nyquist plot of the symmetric cell should compose of a semicircle at high frequency due to the charge transfer at the electrode/electrolyte interface and a Warburg impedance caused by ion diffusion through the electrolyte at the medium frequency. This ideal spectrum was observed for all the symmetric cells and the bulk resistance of the electrolyte was extracted by fitting the equivalent circuit to the measured spectrum. The ion conductivity σ was calculated by the following equation (S-2).

$$\sigma = \frac{d}{R_b A} \qquad \text{(S-2)}$$

Where d, A and R_b are the electrode distance (cm), the active area of the interface between the electrodes and electrolyte (cm^2) and the bulk resistance (Ω), respectively. The active area for the sample using the comb-shaped gold electrode was about 0.0355 cm^2.

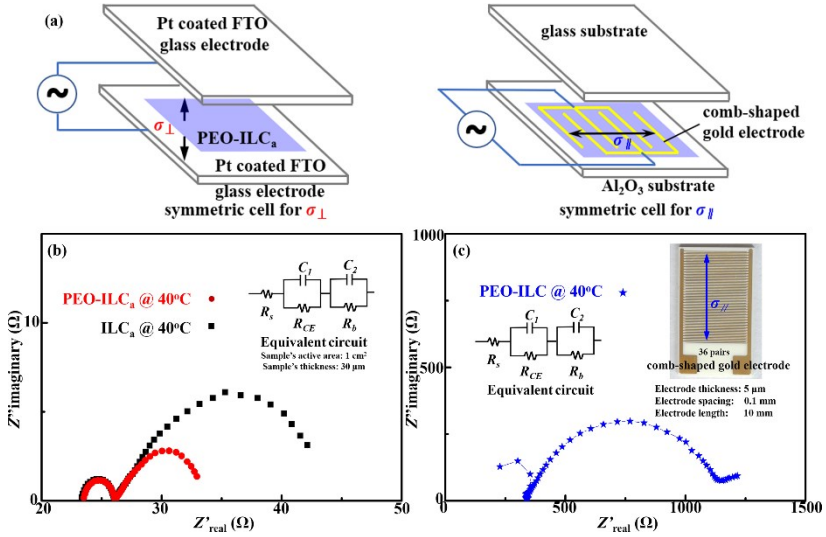

Fig. S7 (a) Schematic illustration of symmetric cells for EIS measurements and the direction of the measured ion conductivity; (b) Nyquist plots of PEO-ILC$_a$ and ILC$_a$ at 40°C for $\sigma_\perp$ (inset is the equivalent circuit. R_S, serial resistance; R_{CE}, interfacial resistance; R_b, bulk resistance); (c) Nyquist plots of PEO-ILC$_a$ at 40°C for $\sigma_{//}$ (insets are the equivalent circuit and image of the applied comb-shaped golden electrode)

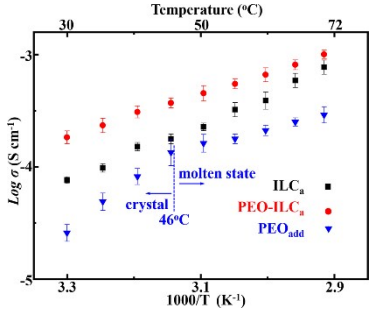

Fig. S8 Temperature dependent ion conductivities of ILC$_a$, PEO-ILC$_a$ and PEO$_{add}$

5. SEM images of the DSSCs

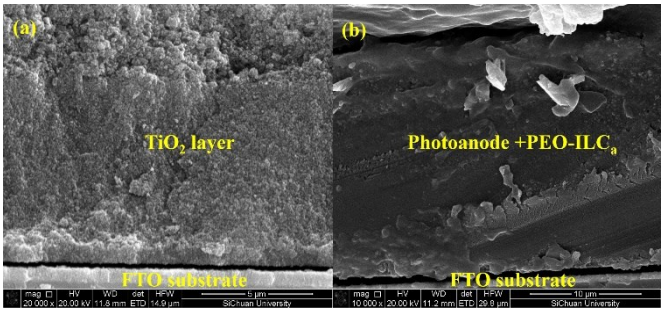

Fig. S9 SEM images of the photoanode (a) and the photoanode with PEO-ILC_a (b)

6. EIS measurements and *IPCE* spectra of the DSSCs

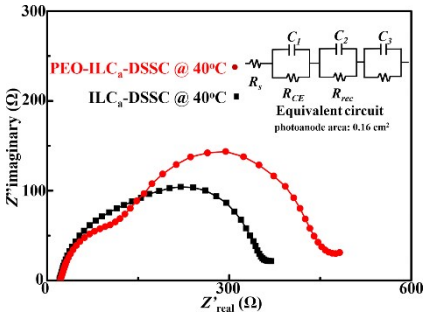

Fig. S10 Nyquist plots of PEO-ILC$_a$-DSSC and ILC$_a$-DSSC at 40°C (Inset is the equivalent circuit R_S, serial resistance; R_{CE}, charge-transfer resistance at the counter electrode/electrolyte interface; R_{rec}, the recombination resistance at the photoanode/electrolyte interface).

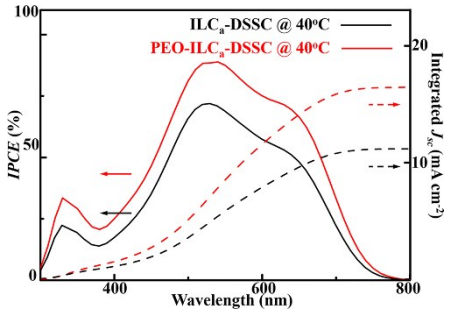

Fig. S11 *IPCE* spectra and the integrated J_{sc} of ILC$_a$-DSSC and PEO-ILC$_a$-DSSC at 40 °C.

The integrated current density J_{sc} from the incident photon-to-current conversion efficiency (IPCE) spectrum was calculated using Eq. (S-3),

$$J_{sc} = \frac{e_0}{hc}\int P_{in}(\lambda)\cdot\lambda\cdot IPCE(\lambda)d\lambda \qquad \text{(S-3)}$$

Where e_0, h, c, λ, $P_{in}(\lambda)$ and IPCE (λ) are the elementary charge, Planck's constant (h=6.63×10^{-34}J s), the speed of light (c=3.0×10^{8}m s^{-1}), the wavelength of the incident light (nm), irradiation intensity of the incident light at λ and the IPCE at λ (W m^{-2}), respectively.

7. Comparisons table of performance and properties

Table S1 Comparisons of performance and properties among the PEO and liquid crystal based electrolytes reported in recent five years

Electrolytes	Redox couple	Efficiency	stability	reference
Liquid crystal based electrolytes	I^-/I_3^-	5.8% @ 30 °C 3.0% @ 90 °C	retained almost original *PCE* after 1000 h	[S3]
	I^-/I_3^- $SeCN/(SeCN)_2$	3.24% @ 30 °C 0.78% @ 30 °C	Not given for the liquid crystal electrolytes	[S4]
	I^-/I_3^-	5.13% @ r.t.	retained almost original *PCE* after 1200 h	[S5]
	thiolate/disulfide	3.2% @ 40 °C 4.1%@ 70 °C	retained 90% of the original *PCE* after 1000 h	[S2]
	thiolate/disulfide	2.2% @ 30 °C	Not given	[S6]
PEO solidified liquid electrolytes	I^-/I_3^-	7.17% @ r.t.	Not given	[S7]
	I^-/I_3^-	6.44% @ r.t.	Not given	[S8]
	I^-/I_3^-	3.9% @ r.t.	Not given	[S9]
	I^-/I_3^-	7.43% @ r.t. 9.12% @ r.t. with further optimization	retained about 90% of the original *PCE* after 500 h	[S10]
	I^-/I_3^-	2.8% @ 50 °C	retained about 90% of the original *PCE* after 1000 h	[S11]
PEO-ILC_a	I^-/I_3^-	**6.4% @ 30 °C** **7.2% @ 70 °C**	retained 85% of the original *PCE* after **5000 h**	This work

Reference

1 X. Li, S. Hsu, *J. Polym. Sci. Pol. Phys. Ed.*, 1984, **22**, 1331.

2 S. Tan, Z. Zhao, S. Wang and Y. Wu, *Electrochim. Acta*, 2018, **288**, 165.

3 D. Högberg, B. Soberats, R. Yatagai, S. Uchida, M. Yoshio, L. Kloo, H. Segawa and T. Kato, *Chem. Mater.*, 2016, **28**, 6493.

4 A. Lennert, M. Sternberg, K. Meyer, R. Costa and D. Guldi, *ACS. Appl. Mater. Interfaces*, 2017, **9**, 33437.

5 S. Cong, Q. Yi, Y. Wang, J. Zhao, Y. Sun and G. Zou, *J. Power Sources*, 2015, **280**, 90.

6 X. Li, Z. Zhao, J. Zhou, C. Wang, Y. Wu and S. Tan, *Chem. Eng. Sci.*, 2020, **221**, 115710.

7 N. Pavithra, D. Velayutham, A. Sorrentino and S. Anandan, *J. Power Sources*, 2017, **353**, 245.

8 J. Ri, J. Jin, J. Xu, T. Peng and K. Ryu, *Electrochim. Acta*, 2016, **201**, 251.

9 D. Sygkridou, A. Rapsomanikis and EliasStathatos, *Sol. Energy Mater. Sol. Cells*, 2017, **159**, 600.

10 S. Venkatesan, I. Liu, J. Lin, M. Tsai, H. Teng and Y. Lee, *J. Mater. Chem. A*, 2018, **6**, 10085.

11 K. Sonigara, J. Vaghasiya, H. Machhi, J. Prasad, A. Gibaud and S. Soni, *ACS Appl. Energy Mater.*, 2018, **1**, 3665.